

Drop dynamics after impact on a solid wall: Theory and simulations

Cite as: Phys. Fluids **22**, 062101 (2010); <https://doi.org/10.1063/1.3432498>

Submitted: 23 September 2009 . Accepted: 21 April 2010 . Published Online: 11 June 2010

Jens Eggers, Marco A. Fontelos, Christophe Josserand, and Stéphane Zaleski



View Online



Export Citation

ARTICLES YOU MAY BE INTERESTED IN

[Capillary effects during droplet impact on a solid surface](#)

Physics of Fluids **8**, 650 (1996); <https://doi.org/10.1063/1.868850>

[Dynamic contact angle of spreading droplets: Experiments and simulations](#)

Physics of Fluids **17**, 062103 (2005); <https://doi.org/10.1063/1.1928828>

[Drop impact and wettability: From hydrophilic to superhydrophobic surfaces](#)

Physics of Fluids **24**, 102104 (2012); <https://doi.org/10.1063/1.4757122>



AIP Conference Proceedings
FLASH WINTER SALE!
50% OFF ALL PRINT PROCEEDINGS
 ENTER CODE **50DEC19** AT CHECKOUT

Drop dynamics after impact on a solid wall: Theory and simulations

Jens Eggers,¹ Marco A. Fontelos,² Christophe Josserand,^{3,4} and Stéphane Zaleski^{3,4}

¹*School of Mathematics, University of Bristol, University Walk, Bristol BS8 1TW, United Kingdom*

²*CSIC-UAM-UC3M-UCM, Instituto de Ciencias Matemáticas (ICMAT), C/Serrano 123, 28006 Madrid, Spain*

³*CNRS, UMR 7190, Institut Jean Le Rond d'Alembert, F-75005 Paris, France*

⁴*UMR 7190, Institut Jean Le Rond d'Alembert, Université Paris 06, F-75005 Paris, France*

(Received 23 September 2009; accepted 21 April 2010; published online 11 June 2010)

We study the impact of a fluid drop onto a planar solid surface at high speed so that at impact, kinetic energy dominates over surface energy and inertia dominates over viscous effects. As the drop spreads, it deforms into a thin film, whose thickness is limited by the growth of a viscous boundary layer near the solid wall. Owing to surface tension, the edge of the film retracts relative to the flow in the film and fluid collects into a toroidal rim bounding the film. Using mass and momentum conservation, we construct a model for the radius of the deposit as a function of time. At each stage, we perform detailed comparisons between theory and numerical simulations of the Navier–Stokes equation. © 2010 American Institute of Physics. [doi:10.1063/1.3432498]

I. INTRODUCTION

Understanding the impact of fluid drops on a solid wall is relevant to a large number of industrial and environmental processes. Examples include printing, cooling of surfaces by sprays, deposition of pesticides or nutrients on plant leaves, or natural rain. Of particular interest is the question of whether the drop will be deposited on the solid surface or whether it will rebound eventually. The latter is particularly likely on water-repellent surfaces, such as plant leaves.¹ To address this question, an understanding of the entire impact process is necessary, as well as to calculate the remaining kinetic energy available for rebound. A large number of theoretical and applied papers are testament to the scientific interest of the problem (see, for example, Refs. 1–10).

Upon impact, the drop begins to spread on the solid surface and the kinetic energy of the drop is converted into surface energy. At the same time, fluid viscosity comes into play, in particular near the solid surface, where we assume a no-slip boundary condition. In this paper, we will consider the case that the fluid is repelled perfectly by the solid, as it is true to a very good approximation for water on plant leaves. This means that the contact angle between the drop and the solid is 180° and wetting properties do not enter the description.¹¹

Thus assuming a spherical drop upon impact, there remain three dimensionless parameters which determine the dynamics

$$\text{We} = \frac{2\rho R U^2}{\gamma}, \quad \text{Re} = \frac{2RU}{\nu}, \quad \text{Fr} = \frac{U^2}{2gR}, \quad (1)$$

which are called the Weber number, Reynolds number, and Froude number, respectively. Here, R is the drop radius ($D=2R$ is the diameter), ρ is the fluid density, ν is the kinematic viscosity, and g is the acceleration of gravity. For high We , the surrounding gas atmosphere provokes instability of the rim of the spreading drop, which renders the motion unsteady and breaks the cylindrical symmetry. This instability can be avoided by reducing the ambient gas pressure by

about a factor of 5 (Ref. 12) below the atmospheric pressure. Additionally, a small air bubble can be entrapped below the drop at impact, owing to the air layer below the drop.^{13–15} However, in the following, we will ignore the effect of rim instabilities and the influence of the surrounding gas.

Our focus in this paper is on the regime of large We , Re , and Fr numbers. For example, for rain, the size and speed varies between $R=0.5$ mm and $U=4.5$ m/s for small drops and $R=2$ mm and $U=9$ m/s for large drops.¹⁶ Thus $(\text{Re}, \text{We})=(4500, 280)$ and $(36\,000, 4500)$, respectively, while $\text{Fr}=2025$ in both cases. The Froude number measures the relative importance of kinetic and gravitational energy on the scale of the drop size. Thus, as long as the drop remains on the plate, gravity can be neglected, as we will do throughout this paper. However, similar arguments do not apply to the Reynolds and Weber numbers. The Weber number measures the relative importance of kinetic and surface energy of the drop. A large We number means that the drop spreads to a maximum radius much greater than its initial value, thus acquiring a large surface area. A large Reynolds number, on the other hand, means that viscous effects are confined to a thin boundary layer close to the solid surface.

Previous modeling efforts largely ignore the small-scale structure that results from the fact that both We and Re are large. For example, in Refs. 2 and 7, the spreading drop after impact is modeled as a pancake of constant thickness, as opposed to a thin film actually observed in the high-speed regime.⁵ In addition, the boundary layer structure is ignored as well, except for a recent paper¹⁷ in which some of the solutions we used were employed independently. Both ingredients are necessary to model high-speed impacts correctly.

In this paper, numerical simulations will be used both as a guide to the proper modeling of impact and to compare to theoretical predictions quantitatively. We simulate the Navier–Stokes equation for the liquid with free surface boundary conditions at the interface (so that no outer fluid is considered) using a method described in detail in Ref. 18. To assure an accurate description of the interface, we use a

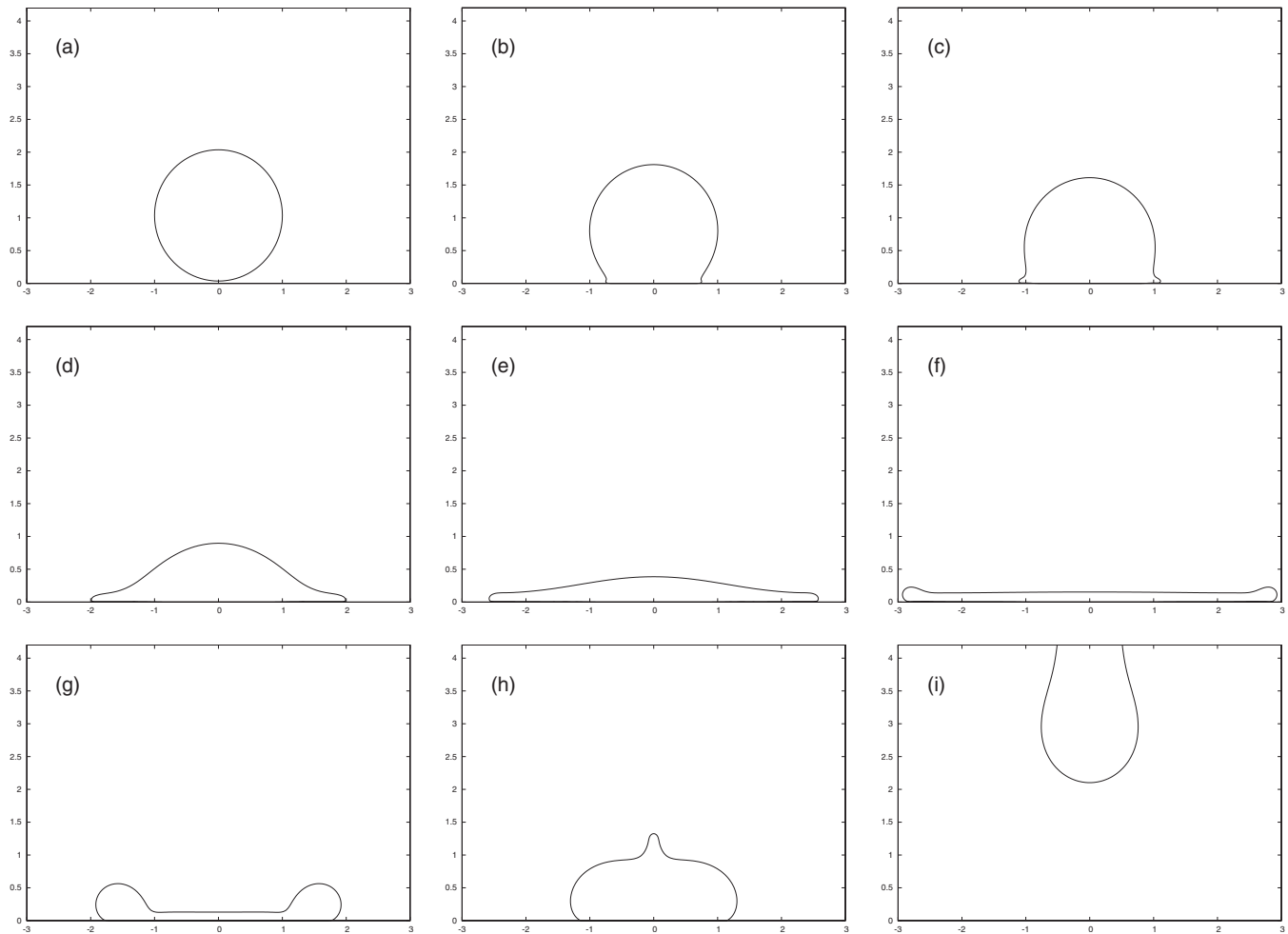


FIG. 1. Snapshots of a drop impacting on a solid surface obtained numerically using the markers method for $Re=400$ and $We=800$. Times of the different snapshots correspond to $t/\tau=0, 0.22, 0.43, 1.3, 2.5, 5.7, 15.8, 21.2$, and 60 from left to right and top to bottom, respectively.

marker method which imposes a hydrophobic (180° contact angle) boundary condition at the contact line between the drop and the plate. This also has the advantage that the usual viscous singularity at a moving contact line is avoided,¹⁹ so the contact angle condition can be enforced on the scale of the mesh. The drop dynamics will be described in cylindrical coordinates r and z , the z -axis being defined by the symmetry axis of the problem, with $z=0$ at the wall. The drop is assumed to remain spherical before it touches the wall at $t=0$. In the simulations, we have been able to vary the Reynolds number from 400 to 8000 and the Weber number from 400 to 16 000, while still being able to resolve all the relevant flow features.

A typical series of snapshots of the drop impact dynamics is shown in Fig. 1 for $Re=400$ and $We=800$. We report times in units of the typical impact time $\tau=R/U$ and lengths are given in units of R . In the first line of Fig. 1, the first stage of impact is shown, during which the drop is strongly deformed near the bottom, while its upper part retains its original shape. In Figs. 1(d) and 1(e), the drop starts to flatten and deforms into a film much thinner than R . In Fig. 1(f), the film has reached its final and remarkably uniform thickness. At the same time, the end has begun to retract and fluid

collects into a rim. Subsequently, retraction continues and fluid collects into the rim which thickens, while the film thickness remains the same, as seen in frame (g). In Fig. 1(h), the radius of the film has shrunk to zero and in the last frame [Fig. 1(i)], the drop is seen to have left the substrate and to hit the upper boundary of the computational domain. The time evolutions of two key quantities derived from the impact dynamics of Fig. 1 are shown in Fig. 2. The contact radius of the drop on the solid substrate illustrates the spreading and subsequent retraction and the height at the center of the drop shows the formation of a thin film, whose thickness remains constant during the retraction phase.

The analytical description of the first stage of impact is particularly difficult, as the drop undergoes a strong deformation and the flow is redirected from a vertical to a horizontal flow direction. The redirection of the flow is driven by very strong pressure gradients, as illustrated in Fig. 3. In agreement with classical impact theory,²⁰ the high pressure region occupies a volume with the same radius as the contact area of the drop with the solid. Using the horizontal momentum balance to such open domain and applying the pressure impact approach,²¹ we obtain that the amplitude of pressure field $P(t)$ in this self-similar region behaves like

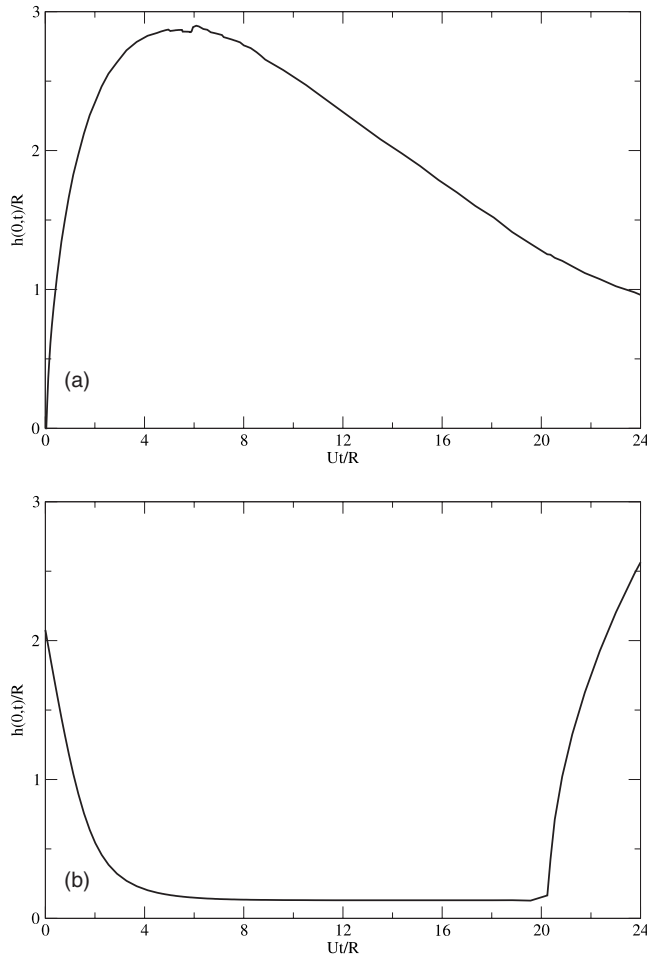


FIG. 2. Time evolution of (a) the radius of the contact area between the drop and the substrate and of (b) the height of the interface on the symmetry axis. The radius and the height are rescaled by the drop radius R and time is shown in units of τ .

$$\frac{P(t)}{\rho U^2} \sim \sqrt{\frac{\tau}{t}},$$

similar to the scaling obtained for the drop impact on a thin liquid film.²² Thus, after time $\tau = R/U$, the high pressure region has spread over the whole drop and the stopping of the original vertical flow is complete. This means that shortly after this time, the maximum pressure in the flow decreases very quickly, as shown in Fig. 4, and the flow in the drop is no longer pressure-driven. Instead, it is described to a good approximation by a simple hyperbolic flow with a rapidly decaying pressure, as suggested in Ref. 23 and described in Sec. II below. This observation permits a universal description of drop impact at high speeds.

In this paper, we will concentrate on times $t > \tau$, during which the drop spreads dynamically and subsequently retracts. We use the abovementioned hyperbolic flow solution as an outer solution of the Euler equation with a free surface, and show that it leads to a similarity solution of drop dynamics; this will be done in Sec. III. There, we will describe the growth of a viscous boundary layer and compare the resulting velocity profile to numerical simulations.

The asymptotic film thickness in the interior of the drop is reached when the free surface meets the viscous boundary layer. Section IV describes the dynamics of spreading and retraction by considering the coupled dynamics of the film and its rim. The rim grows in mass at the expense of the film as the edge of the film retracts relative to the flow speed in the film. The dynamics $R(t)$ of the total drop radius is once more compared to our numerical simulations, using a minimal set of adjustable parameters. Finally in Sec. V, we compare to the results of earlier theories.

II. LIQUID SHEET EXPANSION

We intend to describe the intermediate and long time dynamics of drop impacts. There, the pressure becomes insignificant as a driving force for the flow. This suggests the following hyperbolic flow pattern as the inviscid base flow, following the first interaction period:

$$v_r = \frac{r}{t}, \quad v_z = -\frac{2z}{t}. \quad (2)$$

We note the obvious fact that time can be replaced by $t + t_0$ here and in all of the following expressions. The physical significance of t_0 is the time it takes for the pressure to decay and the hyperbolic flow to establish itself. According to our previous arguments, t_0 is in the order of τ .

The flow (2) is an exact solution of the Euler equations with the pressure distribution $p(z, r, t)/\rho = -3z^2/t^2$. The pressure is thus decaying quickly in time, in agreement with the observation that the flow at intermediate times is no longer pressure-driven. The equation of motion for the convection of the free surface $h(r, t)$ by Eq. (2) is

$$\partial_t h + v_r \frac{\partial h}{\partial r} = v_z. \quad (3)$$

This equation has the similarity solution

$$h(r, t) = \frac{1}{t^2} H\left(\frac{r}{t}\right), \quad (4)$$

valid for any function H . Note that Eq. (4) permits to implement any initial condition for the shape of the drop at time $t=0$. It is an exact solution to the inviscid flow problem apart from the pressure boundary condition, which requires $p = -3h^2(z, t)/t^2$. As h goes down, this pressure quickly becomes insignificant and the boundary condition may be taken as one of vanishing pressure. This is consistent with the fact that at intermediate times, inertia dominates over surface tension, so the physical boundary condition is once more one of constant pressure.

To put the similarity solution (4) to the test, we compare it to our numerical simulations. In Fig. 5 (left), we plot a series of drop profiles for different times in the intermediate regime of drop spreading. We consider two very different Weber numbers $We=800$ and $We=16\,000$ for the Reynolds number $Re=800$. The profiles are first made dimensionless by rescaling with the length $V^{1/3}$, where V is the drop volume. Calling the resulting maximum dimensionless height ℓ ,

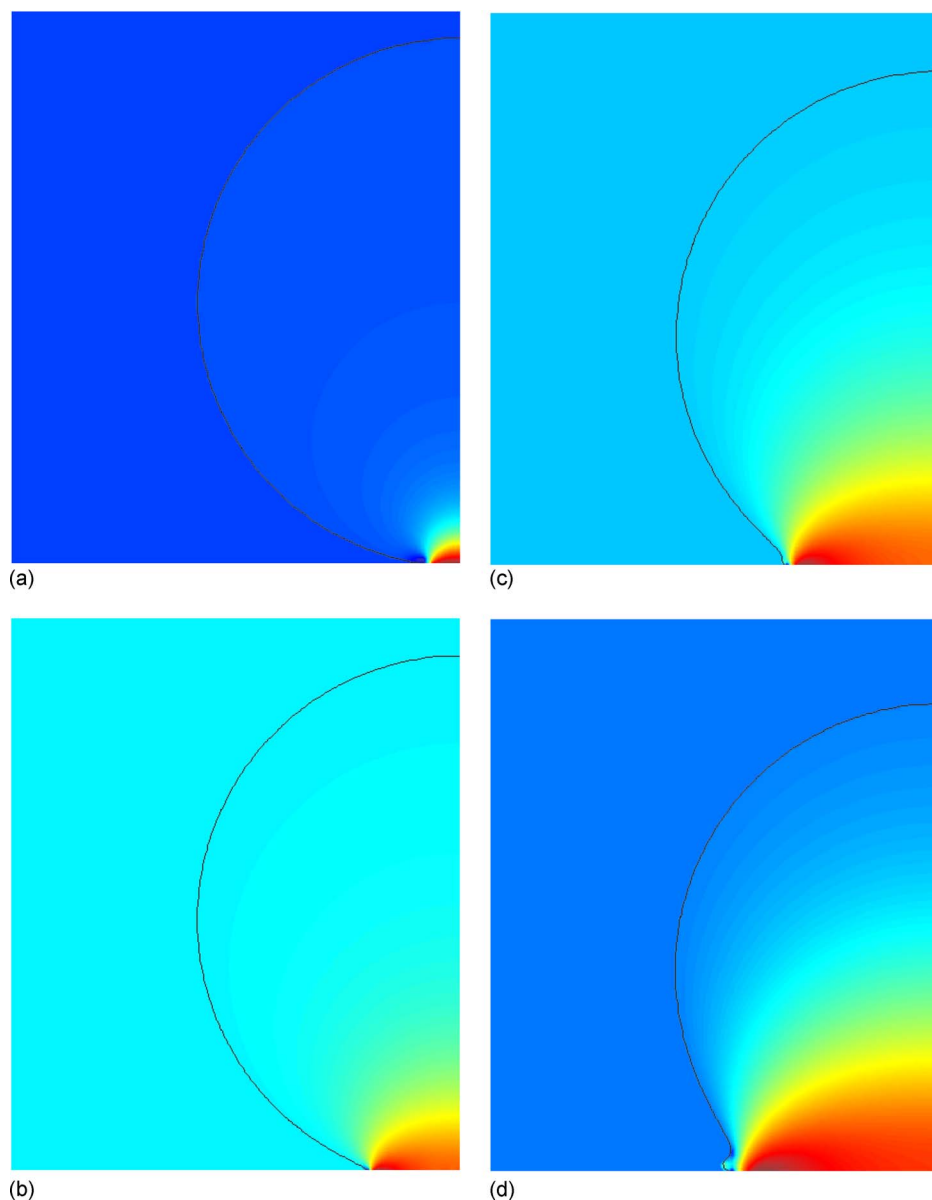


FIG. 3. (Color online) The pressure field corresponding to the same conditions in Fig. 1 for (a) $t/\tau=0.08$, (b) 0.12, (c) 0.2, and (d) 0.29. The shade scale goes from light to dark for increasing values of the pressure.

we divide the height by ℓ and the radius by $\sqrt{\ell}$. The result is equivalent to dividing the physical height by its maximum h_{\max} and the physical radius by $(V/h_{\max})^{1/2}$. As seen in Fig. 5 (right), the collapse to a self-similar profile is quite satisfactory over a period of very significant drop deformation. In both examples, the rescaled profiles for larger times come close to a profile of universal shape, which is well fitted by

$$H_s(x) = 1/(1 + Cx^2)^6, \quad (5)$$

with the constant $C=0.625$. As we vary the Weber number from 800 to 16 000, we see no difference in the self-similar profile, while there is a mild dependence of C on Reynolds number. With this adjustment, Reynolds numbers from 200 to 8000 can be described equally well. This confirms our assertion that the initial (pressure-driven) impact dynamics is forgotten after a time τ and the subsequent evolution is described by the flow (2).

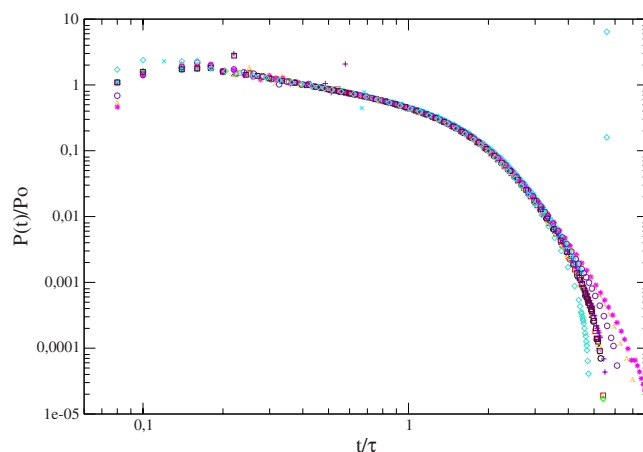


FIG. 4. (Color online) Pressure at the center of impact as function of t/τ for different Reynolds and Weber numbers ranging from 400 to 8000 and from 160 to 80 000, respectively ($P_0=\rho U^2$). The behavior predicted by the small time impact theory is the dashed line. For $t>\tau$, notice that the pressure drops dramatically.

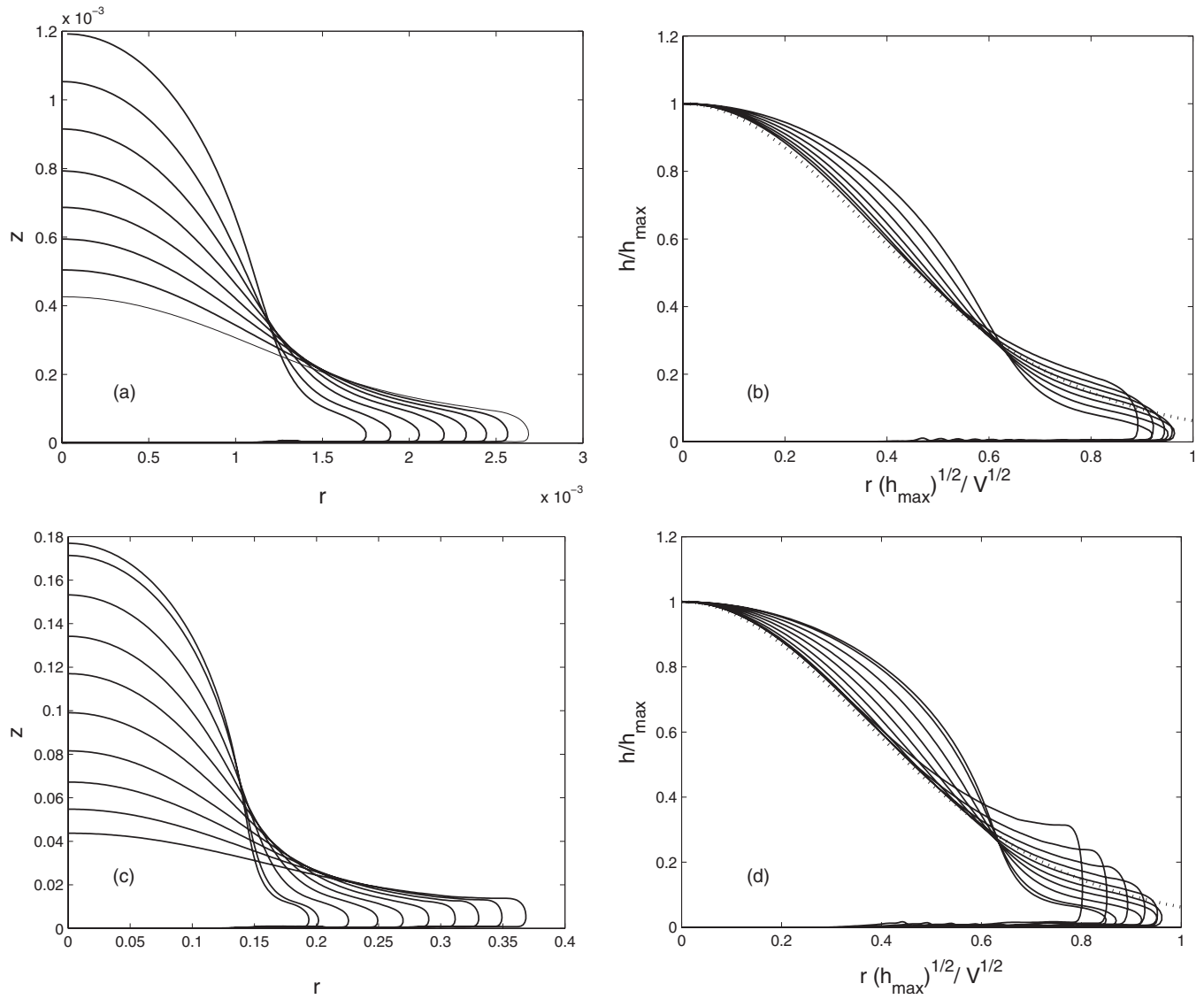


FIG. 5. Top and bottom left: series of drop profiles for different times. Top left for $Re=400$ and $We=400$ for t varying from 0.8 to 2.7. Bottom left: $Re=400$ and $We=8000$ for t varying from 0.9 to 2.3. Right figures show the same profiles rescaled by the maximum height for h and by its square root for r , according to Eq. (4). The axis coordinates in the figures correspond to the numerical mesh. The dashed line shows a fit of the converged rescaled profiles $H_s = 1/(1+Cx^2)^6$, with $C=0.625$ in dimensionless units.

III. BOUNDARY LAYER

In the Sec. II, we described an inviscid outer solution (2), which for large Reynolds numbers will develop a thin boundary layer near the solid surface. If the boundary layer is thinner than the drop thickness, we can neglect the effect of the free surface. Remarkably, solutions of this *time-dependent* boundary layer equations have been studied more than 50 years ago and can be found in Ref. 24; we repeat the axisymmetric version of the analysis here. Moreover, similar calculations have been proposed recently in the same context of drop impacts.¹⁷

The r component of the axisymmetric Navier–Stokes equation reads²⁵

$$\begin{aligned} & \partial_r v_r + v_r \partial_r v_r + v_z \partial_z v_r \\ &= -\partial_r p / \rho + \nu (\partial_r^2 v_r + \partial_z^2 v_r + \partial_r v_r / r - v_r / r^2) \end{aligned} \quad (6)$$

and

$$\partial_r v_r + \partial_z v_z + v_r / r = 0 \quad (7)$$

is the incompressibility condition. According to the boundary layer theory of Prandtl,²⁶ a typical length scale in the z -direction (normal to the solid surface) is smaller by a factor of $1/\sqrt{Re}$ than a corresponding scale in the r -direction. According to Eq. (7), on the other hand, $v_r/v_z = O(\sqrt{Re})$. As a result, all terms on the left hand side of Eq. (6) are of the same order, but of the viscous terms, only the one with the highest number of z -derivatives survives.

Thus the boundary layer equation becomes

$$\partial_r v_r + v_r \partial_r v_r + v_z \partial_z v_r = -\partial_r p / \rho + \nu \partial_z^2 v_r. \quad (8)$$

As usual, the pressure distribution is that of the inviscid problem, which does not have any radial gradients, so it drops out from the equation. To satisfy incompressibility, it is most convenient to look for the stream function ψ

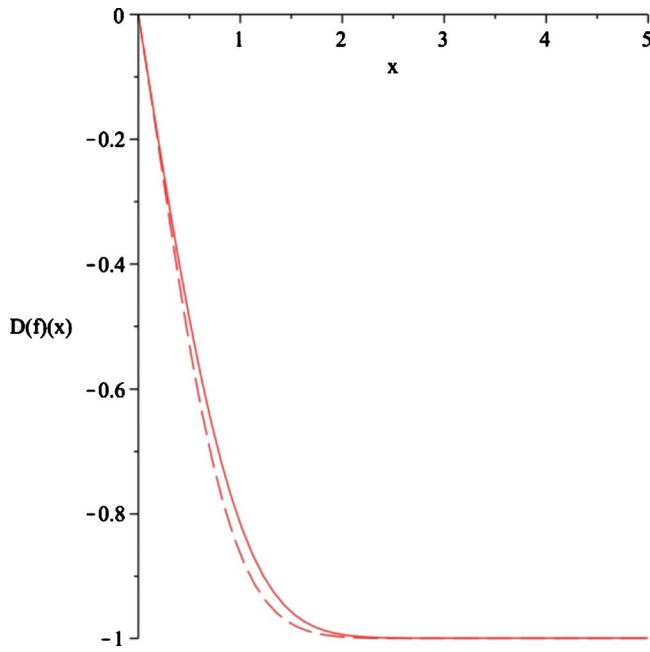


FIG. 6. (Color online) The similarity profile. The dashed line is $f'(\xi) = -1 + \exp\{-\xi - \xi^2\}$.

$$v_r = -\frac{\partial_z \psi}{r}, \quad v_z = \frac{\partial_r \psi}{r}. \quad (9)$$

In the inviscid case, $\psi = -r^2 z/t$. Moreover, the typical length scale for diffusion of vorticity is $\delta = \sqrt{\nu t}$, which suggests the ansatz

$$\psi = \sqrt{\nu} \frac{r^2}{\sqrt{t}} f\left(\frac{z}{\sqrt{\nu t}}\right). \quad (10)$$

For $f(\xi) = -\xi$, the inviscid result is recovered. Inserting Eq. (10) into the boundary layer Eq. (8), we find

$$f' + \eta f''/2 + f'^2 - 2ff'' = -f'''. \quad (11)$$

The boundary conditions are

$$f'(\infty) = -1, \quad f(0) = 0, \quad f'(0) = 0. \quad (12)$$

The numerical solution of Eq. (11), subject to Eq. (12), is shown in Fig. 6. We are not able to solve the equation exactly but report an empirical function which matches the true solution closely.

We now compare this boundary layer solution with our numerical simulations of the impacting drop. The z component of the velocity field is given in the boundary layer theory by

$$v_z = 2\sqrt{\frac{\nu}{t+t_0}} f'\left[\frac{z}{\sqrt{\nu(t+t_0)}}\right], \quad (13)$$

so that its derivative becomes

$$\partial_z v_z = \frac{2}{t+t_0} f'\left[\frac{z}{\sqrt{\nu(t+t_0)}}\right].$$

Since the minimum of f' is -1 from the asymptotic matching, we can write for any time

$$\partial_z v_z = (-M)f'\left[\frac{z}{\sqrt{2\nu(-M)}}\right], \quad (14)$$

where M is the minimum of $\partial_z v_z$. Therefore, rescaling the numerical velocity derivative profiles by $-M$ and the vertical coordinate z by $\sqrt{2\nu(-M)}$, all profiles should collapse onto the master curve f' . This is true for any time and or any value of the parameters Re , We .

Figure 7 (left) shows the numerical profiles $\partial_z v_z$ for two different sets of parameter values at different times. On the right, the profiles which have been rescaled according to Eq. (14) are compared to the theoretical boundary layer profile. We find good collapse as well as good agreement with the predicted similarity profile $f'(\xi)$. We have also checked the collapse for Reynolds numbers between 200 and 8000 and Weber numbers between 400 and 16 000, and found the results comparable to those shown in the two representative examples of Fig. 7.

Note that we have assumed the boundary layer to remain laminar, which we believe to be realistic. Namely, according to Ref. 27, p. 95, the critical Reynolds number Re_δ based on the *boundary layer thickness* is typically 400. On account of the smallness of δ , Re_δ is much smaller than Re , and well below the critical value. We will give a more quantitative estimate below.

IV. RIM DYNAMICS

We now put all the information gathered so far together to develop a coupled system of equations modeling the rim and film dynamics (see the sketch of the model in Fig. 8). Our approach is similar to the classical Taylor and Culick method to describe receding liquid sheets.^{28,29} It has already been used in the context of drop impact but without taking into account the viscous layer explicitly.⁹

We assume that the velocity field in the film is Eq. (2), but with a shift in the z -direction to account for the viscous boundary layer thickness $h_l(t)$

$$U(r, z, t) = (u_r, u_z) = \left\{ \frac{r}{t+t_0}, -\frac{2[z-h_l(t)]}{t+t_0} \right\} \Theta[z-h_l(t)]. \quad (15)$$

Here, $\Theta(\cdot)$ is the Heaviside function. We thus suppose that most of the fluid is at rest inside the boundary layer. From the profile of f shown in Fig. 6, we infer that the viscous layer is of order unity in boundary layer coordinates, and thus we will use the estimate $h_l(t) \approx \sqrt{\nu t}$. When this boundary layer reaches the height of the film, the film ceases to thin, so we define an effective thickness below which there is no more motion

$$h_m(t) = \min[h_l(t), h(t)]. \quad (16)$$

Using this idea, one can derive an estimate for the asymptotic film thickness h_f at which the drop motion stops in the inner region of the drop. Namely, from the scaling of the inviscid solution (4), one derives the estimate

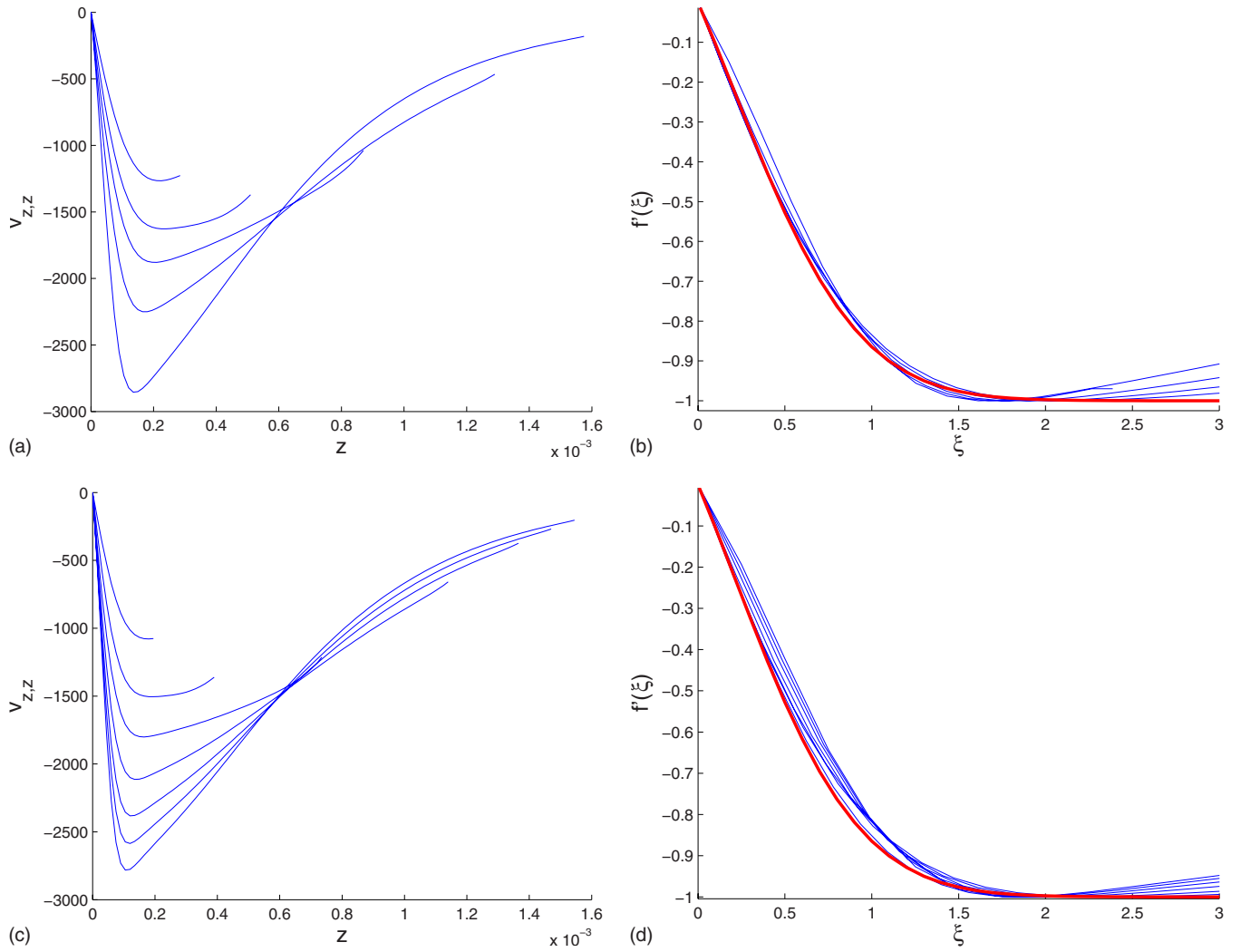


FIG. 7. (Color online) Numerical profiles of the derivative of vertical velocity $\partial_z v_z$ on the symmetry axis for $Re=400$, $We=800$ (top figures) and $Re=800$, $We=4000$ (bottom figure) at different dimensionless times t/τ ranging from 0.2 to 3 in the first case and from 2 to 8 in the second case. The top and bottom left figures show the numerical profiles, while the top and bottom right figures show the same profile rescaled according to formula (14). The thick line in the right figures indicate the approximated theoretical boundary layer $f'(\xi) = -1 + \exp\{-\xi - \xi^2\}$.

$$h(t) \approx \frac{R^3}{U^2 t^2}. \quad (17)$$

At some critical time t_f , the drop thickness will have reached the boundary layer thickness $h(t_f) = \sqrt{\nu t_f}$. The value of h at this time gives the film thickness

$$h_f \approx \frac{R}{Re^{2/5}}, \quad (18)$$

which becomes very thin for large Re , as expected. If we base the estimate of the boundary layer Reynolds number Re_δ on h_f as an upper limit, we obtain $Re_\delta \approx Re^{3/5}$. This is about 200 even for the extremely high Reynolds number of 8000, still well below the critical value of 400.²⁷

The rim dynamics is obtained by writing the mass and momentum balance for the rim located at $R(t)$ and moving at speed $U(t)$. We use the following simplified description: a layer of thickness $h_m(t)$ inside the film (near the wall) is at rest. The remainder $h(t) - h_m(t)$ of the film moves with speed

$U_f = u_r(R(t), h(t), t)$ in the radial direction at the rim position. With these simple ingredients, volume conservation becomes

$$\frac{dV}{dt} = 2\pi R(t) \{ [h(t) - h_m(t)] U_f - h(t) U(t) \}, \quad (19)$$

where $V(t)$ is the volume of the rim. Momentum conservation can be written as

$$V(t) \frac{dU}{dt} = 2\pi R(t) \{ [h(t) - h_m(t)] [U_f(t) - U(t)]^2 + h_m(t) U(t)^2 - 2\gamma/\rho \}. \quad (20)$$

Here, the first and second terms on the right come from the acceleration of the fluid inside the film to the speed of the rim, for the upper layer and the viscous layer, respectively. The third term comes from the pull of the film on the rim, exerted by surface tension. This is, of course, the term responsible for retraction. In the case of a 180° contact angle to be considered here, the force per unit length is 2γ . In principle, one can generalize to a finite contact angle, if one

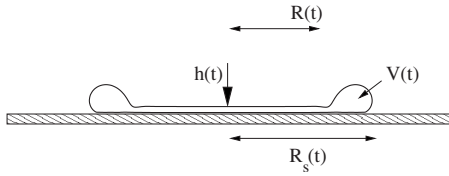


FIG. 8. A sketch of a drop after impact at high speed, so that both Re and We are large. The film thickness is $h(t)$, the radius of the film is $R(t)$, the volume of the rim is $V(t)$, and the total drop radius is $R_s(t)$.

replaces the factor of 2 by $1 - \cos(\theta_{ap})$, where θ_{ap} is the apparent contact angle.¹¹ Finally, the kinematic conditions for the rim position and the film height follow as

$$\frac{dR}{dt} = U(t), \quad \frac{dh}{dt} = u_z[0, h(t), t]. \quad (21)$$

We now compare the model Eqs. (19)–(21) to our numerical simulations. Initial conditions are estimated at $t = \tau$ using simple geometrical arguments. The comparisons are based on the full drop radius R_s , which we consider to be the sum of $R(t)$ and the rim diameter $2R_r(t)$

$$R_s(t) = R(t) + 2R_r(t). \quad (22)$$

Our numerical simulations show that up to $t \approx \tau$, and at sufficiently high impact speeds, R_s depends neither on We nor on Re . At time $t = \tau$, we thus consider the drop to be a pancake of height $h(\tau) = R/2$ and of radius $R\sqrt{8/3}$, as demanded by volume conservation. We estimate the volume $V(\tau)$ of the rim as the edge of this pancake, with the thickness being half of the height

$$V(\tau) = \frac{\pi R^3}{2} \left(\sqrt{\frac{2}{3}} - \frac{1}{16} \right). \quad (23)$$

Further on, the rim radius R_r is related to the rim volume by considering the rim a torus

$$V(t) = 2\pi^2 R(t) R_r^2(t). \quad (24)$$

Finally, three parameters still need to be specified to compare the output of the model to the numerical simulations: the time t_0 appearing in the inviscid velocity field Eq. (15) and two parameters determining the effective boundary layer thickness h_l

$$h_l(t) = \alpha \sqrt{\nu(t + t_1)}. \quad (25)$$

Here, t_1 indicates the time delay between the impacting time and the growth of the boundary layer. The prefactor α in Eq. (25) expresses the lack of mass flux in the film due to the boundary layer. We adjust these three parameters only *once*, for a particular pair of (Re, We) . The same parameters will then be used to predict the time dependence of $R_s(t)$ for a wide range of other values. The three dimensionless parameters t_0/τ , t_1/τ , and α have been determined as a best fit to R_s for the parameter values $Re=800$ and $We=800$, as shown in Fig. 9; we find

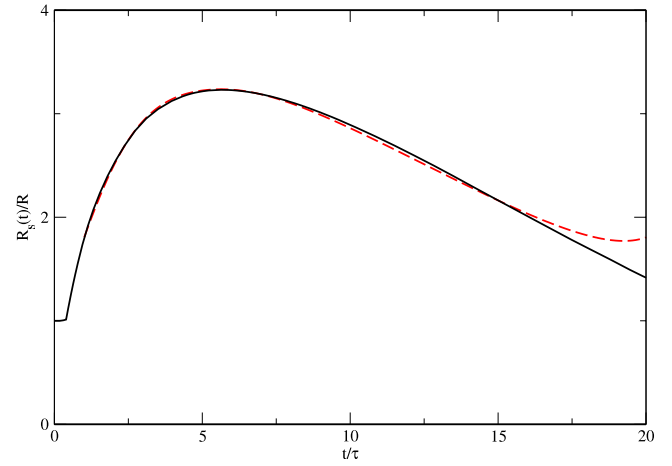


FIG. 9. (Color online) The total drop radius $R_s(t)$ as function of time of an impacting drop with $Re=We=800$. The line is the numerical simulation and the dashed line shows the model output. The free parameters [Eq. (26)] have been fitted to obtain the best possible fit of the experiment.

$$\alpha = 0.9, \quad t_0/\tau = 0.35, \quad t_1/\tau = 0.2. \quad (26)$$

In particular, α can be compared to our boundary layer analysis (7), where one can estimate α as

$$\alpha_{th} = \int_0^\infty [1 + f'(\xi)] d\xi = 0.55. \quad (27)$$

However, in view of the simplifying assumptions of our model, Eq. (27) cannot be expected to provide a perfect description of the effective film thickness. Instead, we have used α as an adjustable parameter and found $\alpha=0.9$, which is reasonably close to the theoretical value.

A first observation is that the model predicts the rim size and its mass to grow only during the retracting regime of the drop, as shown in Fig. 10. This implies that simplified models, which describe the drop as a pancake of uniform thickness, capture the essential ingredients of the drop dynamics during expansion. During retraction, on the other hand, such a simple description is no longer valid, as the film in the center of the drop becomes very thin. As a result, most of the mass is eventually contained in the rim [see Fig. 10 (right)]. Now keeping the parameters in Eq. (26) fixed, the model shows good agreement with simulations as shown in Fig. 11 for Weber and Reynolds numbers varying from 400 to 16 000 and from 800 to 8000. Given the simplicity of the model, this demonstrates remarkably good agreement with the full numerical simulations of the drop impact; in particular, the typical time scale of the evolution is well captured by the model over a wide range of parameters.

V. DISCUSSION

As we demonstrated above, our model gives a quantitative description of the drop dynamics over the entire period of expansion and retraction and for a very wide range of parameter values. We now use this model to extract the universal (scaling) behavior of the dynamics of drop impact and compare it to direct numerical simulations where available.

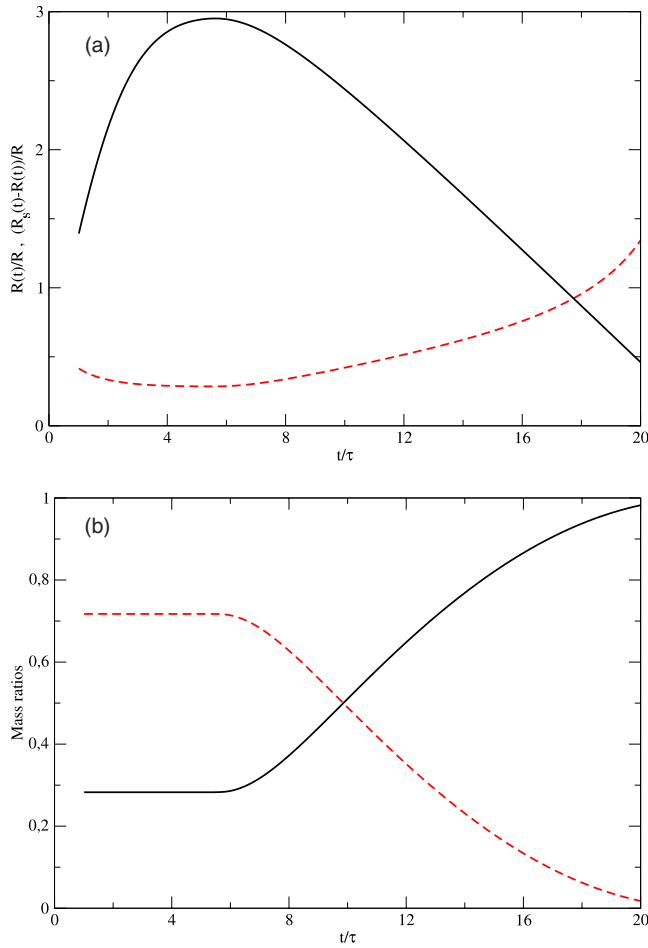


FIG. 10. (Color online) (a) The rim radius $[R_s(t) - R(t)]/R$ (dashed line) and the spreading drop radius $R(t)/R$ (solid line) as function of dimensionless time t/τ . (b) The mass (normalized by the total mass $M_0 = 4\rho\pi R^3/3$) in the rim (solid line) and the one in the film (dotted line) are drawn as functions of time. Both figures show that the rim grows only during the retraction phase of the drop.

In fact, a major advantage of our simplified model description is that it permits to describe parameter regimes in (Re, We) space not accessible by numerical simulation. Namely, if the impact speed becomes too high, certain flow features can no longer be resolved. We will focus on three characteristic quantities of the impact, namely, the minimal film thickness h_f reached during the impact, the maximum spreading radius R_m which we define as the maximum of R_s over time, and the retraction dynamics.

A. Minimal film thickness

In Fig. 12 we show that the minimal film thickness does obey the predicted law (18). Good agreement is also exhibited with the direct numerical simulation cases available. The agreement is significantly better than with the alternative scaling law $h_f \propto Re^{-1/2}$, discussed elsewhere by two of us.³⁰ Such latter scaling arises if one neglects the effect of the initial hyperbolic flow (2) and, in that case, the film thickness scales simply like the thickness of a viscous boundary layer. In the discussion in Ref. 30, the variation in the Reynolds

number was not large enough to exclude the $Re^{-1/2}$ against the $Re^{-2/5}$. The use of our model therefore allows us to discriminate unambiguously between the two theories.

B. Maximal spreading radius

We now turn to the maximum spreading radius R_m , for which numerous theoretical models have been proposed. For large Re and We numbers, two regimes may be assumed: one where viscosity may be neglected so that surface tension selects R_m , the other for which viscous dissipation dominates surface tension, and the maximal radius R_m appears as a balance between inertia and viscosity. As we will see below, the crossover between the two regimes depends on the interplay between viscous and capillary effects, so that the dependence on Re and We can be gathered into a single scaling relation. In the viscous regime, most of the initial kinetic energy will be lost to viscous dissipation. In that case, one obtains for the maximum spreading radius^{7,31}

$$\frac{R_m}{R} \sim C_v Re^{1/5}, \quad (28)$$

where C_v is a prefactor of order 1. In an analytical model where the drop dynamics is described as an expanding pancake, it can be calculated exactly:³¹ $C_v = 1.113$.

When viscosity can be neglected (apart from the boundary layer that we have taken into account in our description), the maximum radius is determined by a balance between inertia and surface tension. Two different scaling laws have been proposed for this regime in the $Re \rightarrow \infty$ limit. The first is obtained by calculating the radius for which the initial kinetic energy is converted completely into surface energy, giving in the large We regime³²

$$\frac{R_m}{R} \sim \left(\frac{We}{6} \right)^{1/2}. \quad (29)$$

Refinements of this theory account for corrections due to viscous dissipation⁹ or contact angle dynamics.³³ On the other hand, an alternative scenario has been suggested recently⁷ for the same regime. The drop is modeled as a pancake flattened by an *effective* gravity. The thickness is thus determined by a capillary length, the usual expression being replaced by an “impact capillary length” $\lambda = \sqrt{\gamma R / (\rho U^2)}$. Using volume conservation, this gives

$$\frac{R_m}{R} \sim \left(\frac{8}{9} We \right)^{1/4}. \quad (30)$$

The two regimes, viscous and capillary dominated, can be condensed into two scaling relations depending on the two different capillary models (29) and (30). If the kinetic energy transfer into capillary energy is valid [cf. Eq. (29)] the spreading radius can be written as

$$\frac{R_m}{R} \propto Re^{1/5} f_c(We Re^{-2/5}) \quad (31)$$

and the relations (28) and (29) impose that the function f_c satisfies

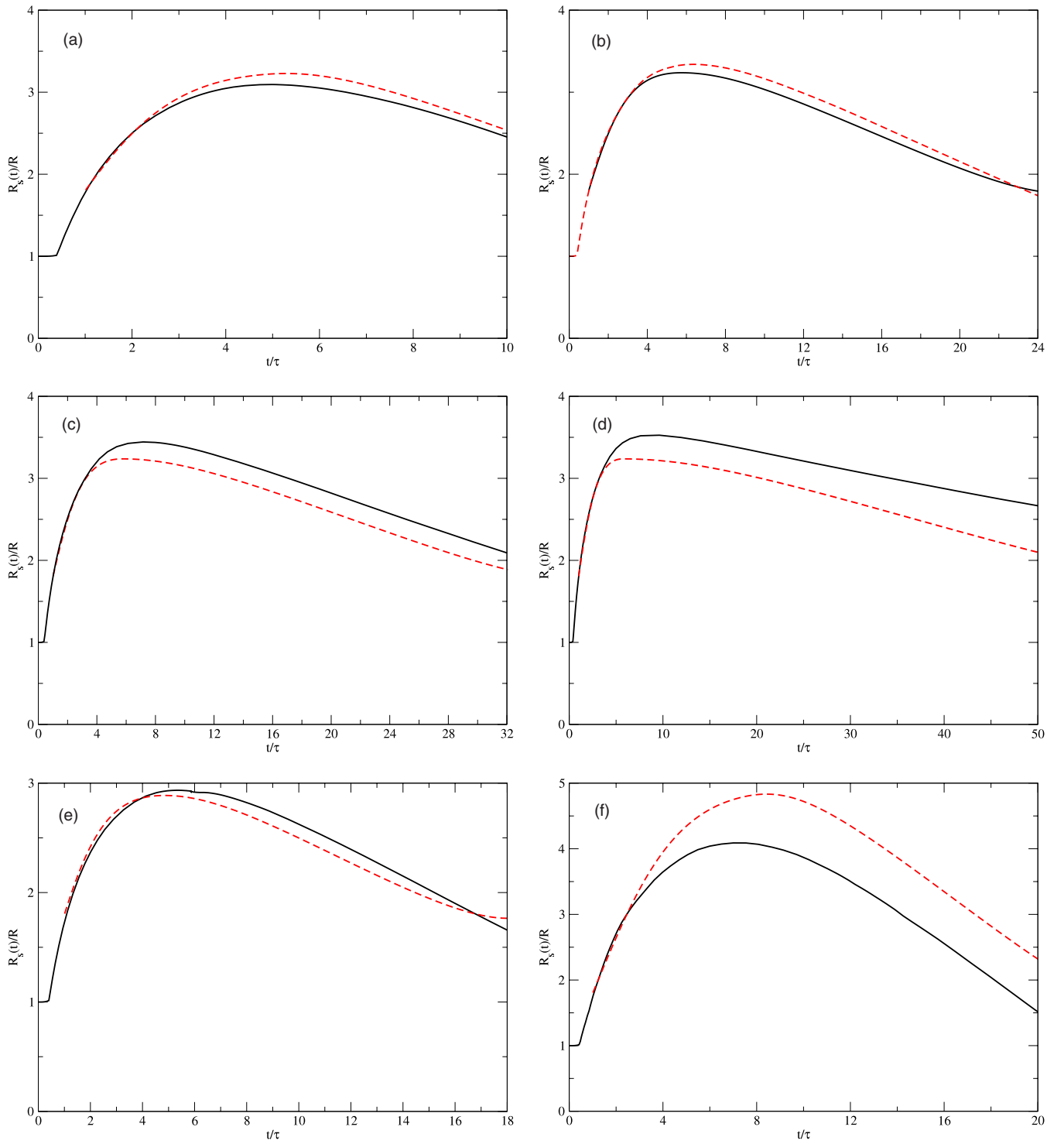


FIG. 11. (Color online) The radius $R_s(t)/R$ as function of time t/τ , for a variety of impact parameters (Re, We) (a) (800,400), (b) (800,1600), (c) (800,4000), (d) (800,16000), (e) (400,800), and (f) (8000,800). The continuous line shows the numerical simulation and the dashed lines the results of the simplified model.

$$\lim_{x \rightarrow \infty} f_c(x) = C_v \quad \text{and} \quad \lim_{x \rightarrow 0} f_c(x) \sim \sqrt{\frac{x}{6}}.$$

$$\frac{R_m}{R} \propto \text{Re}^{1/5} f_p(\text{WeRe}^{-4/5}). \quad (32)$$

On the other hand, for the effective gravity theory (30), the spreading radius can be condensed into

Now the scaling function f_p needs to satisfy the following limits:

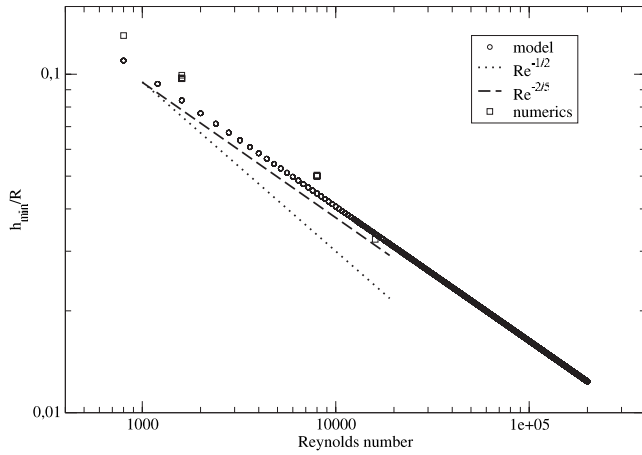


FIG. 12. The minimum radius h_f/R of the film as a function of the Reynolds number obtained using the model (circles) for Weber varying between 100 and 4000 and compared to numerical simulations of the full equations (square). The predicted law $h_f \approx R/Re^{2/5}$ is the dashed line, while the $Re^{-1/2}$ law is the dotted line for comparison.

$$\lim_{x \rightarrow \infty} f_p(x) = C_v \quad \text{and} \quad \lim_{x \rightarrow 0} f_c(x) \sim \left(\frac{8}{9}x\right)^{1/4}.$$

These two relations have the same behavior in the viscous regime, while they differ clearly in the inviscid limit. Again, the simplified model developed here can help to discriminate between the two models (29) and (30). Indeed, Fig. 13 compares the maximum radius obtained with the model to the scaling relations (31) in Fig. 13(a) and (32) in Fig. 13(b).

We observe that Eq. (31) gives a good description of the spreading [Fig. 13(a)], while Eq. (32) [cf. Fig. 13(b)] does not work for small impact parameter $x = We/Re^{4/5}$, for which the different results do not collapse onto a single curve. In addition, we observe that the prefactor in the scaling law is reasonably well predicted by the theory for the capillary law (31), while it is poorer for the other relation (32). The apparent contradiction with the experimental results of Ref. 7 is explained by the fact that only an intermediate regime was investigated, where R_m/R varies between 1.5 and 4 only. Over such a small range, one cannot reliably discriminate between the two regimes (29) and (30). Our model therefore suggests that in the limit of small viscosity, the maximum spreading radius is controlled by a balance between kinetic energy and capillarity, and is not described by the effective gravity theory.

C. Retraction dynamics

Finally, the model also describes the receding dynamics of the drop, at least up to the point where the film radius $R(t)$ goes to zero. As shown in Fig. 11, the model captures the retraction dynamics quite well. The numerics and the model both show that a regime of almost constant retraction velocity (denoted by V_{ret}) is reached during retraction. This velocity is slower at the onset of the retraction because the rim needs first to be accelerated and at the final stage of the retraction, before the rebound of the drop, where the drop cannot anymore be described as a thin film connected to a growing rim but rather as a thick cylindrical structure [see Fig. 1(h)]. The retraction dynamics is crucial for our under-

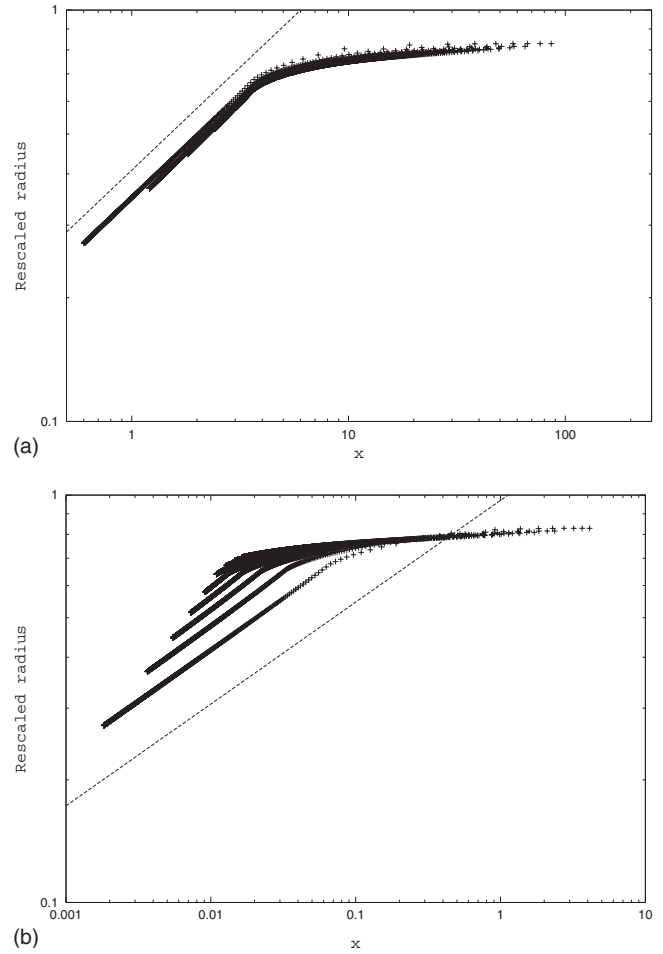


FIG. 13. A test of the two scaling relations (31) (left) and (32) (right), using R_m as calculated from the model. The rescaled maximum radius $(R_m/R)/Re^{1/5}$ is plotted (a) as a function of $x = We/Re^{2/5}$; the expected behavior for small x , $\sqrt{x}/6$, is indicated in dotted line; (b) as function of $x = We/Re^{4/5}$, again showing the expected behavior for small x , $(8x/9)^{1/4}$ (dotted line).

standing of drop rebound or when thermal effects (Marangoni flows or solidification) are considered.³⁴ Experimentally, two regimes have been observed:³⁵ the first one is dominated by a balance of capillarity and inertia and is characterized by the following relation for the retraction rate:³⁵

$$V_{\text{ret}}/R_m = \sqrt{\frac{3\gamma}{2\rho R^3}} = \sqrt{\frac{3}{We} \frac{U}{R}}. \quad (33)$$

This effective retraction rate V_{ret}/R_m is simply obtained by estimating the Taylor–Culick retracting velocity using the minimal film thickness h_f . This Taylor–Culick can simply be deduced from Eq. (20), considering that in the retracting dynamics $h(t) = h_m(t) = h_f$ and $dU/dt = 0$. It gives

$$V_{\text{ret}} = \sqrt{\frac{2\gamma}{\rho h_f}}.$$

Assuming that the drop is close to a pancake at its maximum radius, as suggested above by Fig. 10, mass conservation imposes $\pi h_f R_m^2 \sim \frac{4}{3} \pi R^3$, which gives the relation (33)

$$V_{\text{ret}} = R_m \sqrt{\frac{3\gamma}{2\rho R^3}}.$$

The second regime corresponds to a viscous-capillary balance close to the contact line and does not apply to the case of a 180° contact angle, considered by us. Figure 14(a) shows the maximum velocity during the retraction regime obtained within our model as a function of the Weber number for different Reynolds numbers. As expected on the basis of the capillary retraction theory (33), these results collapse onto a single curve when the retraction rate is considered in Fig. 14(b). The retraction rate is V_{ret}/R_m , which, in our non-dimensionalization, translates into $RV_{\text{ret}}/(R_m U)$. According to Eq. (33), it is expected to scale like $We^{-1/2}$, as confirmed in the figure.

D. Conclusions

In summary, in this paper we have developed a quantitative model for the description of high-speed, hydrophobic drop impact. We disregard all effects of the external air atmosphere, which is justified in a moderate vacuum. The drop evolution is divided into the following stages:

- (i) initial inviscid spreading,
- (ii) boundary layer growth and formation of a film,
- (iii) film spreading, and
- (iv) rim formation and retraction.

For each stage and/or aspect of the flow, we develop an approximation based on the Navier–Stokes equation, each of which is tested against our full numerical simulations. We then use our understanding of each part of the solution to develop a complete model of the impact process, which describes the time evolution of key parameters such as the drop radius during expansion and retraction. Again, the results agree favorably with numerical simulation.

Our key observations are the following:

- (i) After a time R/U , the fluid motion is well described by a time-dependent, hyperbolic flow, bounded by a viscous boundary layer near the wall.
- (ii) The thickness of the boundary layer grows like $\delta = \sqrt{\nu t}$.
- (iii) The drop stops thinning when the free surface reaches the boundary layer thickness; as a result, the drop spreads into a thin film of thickness $f_f \approx R/Re^{2/5}$.
- (iv) The dynamics of the drop radius $R(t)$ during spreading and retraction is described by a thin film, bounded by a toroidal rim.
- (v) For high speeds, the maximum spreading radius R_m behaves like $R_m/R \propto We^{1/2}$.
- (vi) The retraction velocity V_{ret} of the rim scales like $V_{\text{ret}}/R_m \propto UWe^{-1/2}/R$.

Each of the predictions of the model are checked against full numerical simulations, yielding a rather complete description of the complex dynamics of high-speed drop impact.

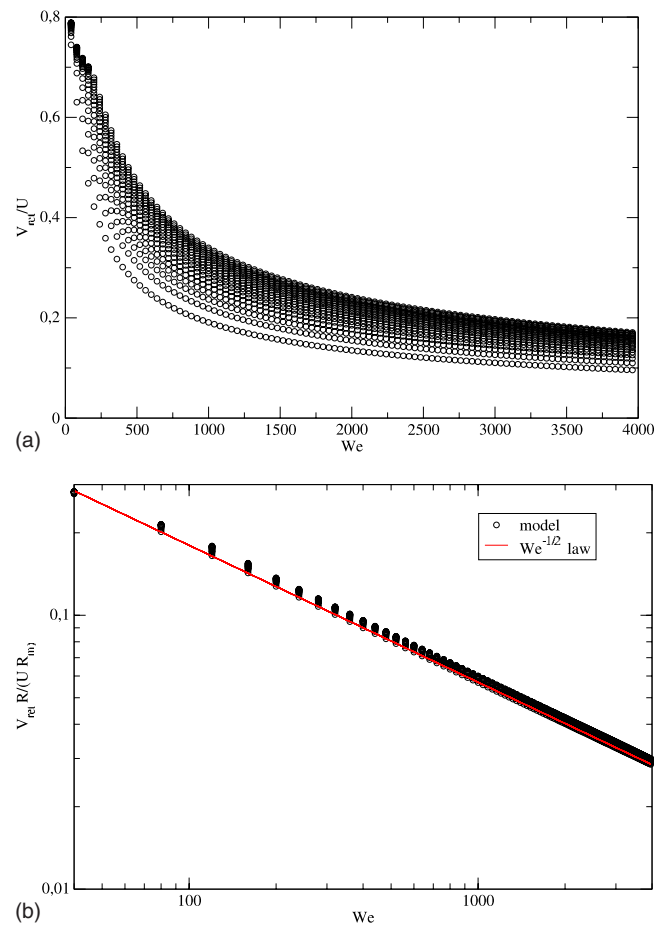


FIG. 14. (Color online) Retraction velocity measured in the model as the maximum velocity reached during the retraction regime (a) V_{ret}/U is shown as a function of Weber number for different Reynolds numbers. (b) According to the theory balancing inertia and capillarity [Eq. (33)], all the curves collapse when the retraction rate $RV_{\text{ret}}/(R_m U)$ is considered. The line shows the fit $RV_{\text{ret}}/(R_m U) = 2/\sqrt{We}$ to be compared to the Taylor–Culick retraction rate (33) $RV_{\text{ret}}/(R_m U) = \sqrt{3/We}$.

It is also interesting to discuss the possible extension of this approach to the general case of drop impact on nonhydrophobic surfaces. If the contact angle θ_e is not 180° , mainly two effects have to be incorporated: the surface force on the rim is different and an additional dissipation is present as the contact line moves.^{11,36} While the surface tension action 2γ on the rim can be simply replaced in Eq. (20), as discussed above, accounting for the contact line viscous dissipation is more complex and should be the subject of further works.

ACKNOWLEDGMENTS

It is our pleasure to thank Stéphane Popinet for enlightening discussions on drop impacts. M. A. Fontelos acknowledges the Ministerio de Ciencia for its support through Grant No. MTM2008-03255 and C. Josserand acknowledges the financial support of the Agence Nationale de la Recherche through Grant No. ANR-09-JCJC-0022 (ANR “Deformation”).

- ¹V. Bergeron, D. Bonn, J.-Y. Martin, and L. Vovelle, "Controlling droplet deposition with polymer additives," *Nature (London)* **405**, 772 (2000).
- ²M. Pasandideh-Fard, Y. M. Qiao, S. Chandra, and J. Mostaghimi, "Capillary effects during droplet impact on a solid surface," *Phys. Fluids* **8**, 650 (1996).
- ³H.-Y. Kim, Z. C. Feng, and J.-H. Chun, "Instability of a liquid jet emerging from a droplet upon collision with a solid surface," *Phys. Fluids* **12**, 531 (2000).
- ⁴M. Bussmann, S. Chandra, and J. Mostaghimi, "Modeling the splash of a drop impacting on a solid surface," *Phys. Fluids* **12**, 3121 (2000).
- ⁵Y. Renardy, S. Popinet, L. Duchemin, M. Renardy, S. Zaleski, C. Josserand, M. A. Drumright-Clarke, D. Richard, C. Clanet, and D. Quéré, "Pyramidal and toroidal water drops after impact on a solid surface," *J. Fluid Mech.* **484**, 69 (2003).
- ⁶D. Richard and D. Quéré, "Bouncing water drops," *Europhys. Lett.* **50**, 769 (2000).
- ⁷C. Clanet, C. Béguin, D. Richard, and D. Quéré, "Maximal deformation of an impacting drop," *J. Fluid Mech.* **517**, 199 (2004).
- ⁸R. Rioboo, M. Marengo, and C. Tropea, "Time evolution of liquid drop impact onto solid, dry surfaces," *Exp. Fluids* **33**, 112 (2002).
- ⁹I. V. Roisman, R. Rioboo, and C. Tropea, "Normal impact of a liquid drop on a dry surface: Model for spreading and receding," *Proc. R. Soc. London, Ser. A* **458**, 1411 (2002).
- ¹⁰D. Bartolo, C. Josserand, and D. Bonn, "Singular jets and bubbles in drop impact," *Phys. Rev. Lett.* **96**, 124501 (2006).
- ¹¹D. Bonn, J. Eggers, J. Indekeu, J. Meunier, and E. Rolley, "Wetting and spreading," *Rev. Mod. Phys.* **81**, 739 (2009).
- ¹²L. Xu, W. W. Zhang, and S. R. Nagel, "Drop splashing on a dry smooth surface," *Phys. Rev. Lett.* **94**, 184505 (2005).
- ¹³S. T. Thoroddsen, T. G. Etoh, K. Takehara, N. Ootsuka, and A. Hatsuki, "The air bubble entrapped under a drop impacting on a solid surface," *J. Fluid Mech.* **545**, 203 (2005).
- ¹⁴A. A. Korobkin, A. S. Ellis, and F. T. Smith, "Trapping of air in impact between a body and shallow water," *J. Fluid Mech.* **611**, 365 (2008).
- ¹⁵S. Mandre, M. Mani, and M. P. Brenner, "Precursors to splashing of liquid droplets on a solid surface," *Phys. Rev. Lett.* **102**, 134502 (2009).
- ¹⁶A. F. Spilhaus, "Drop size, intensity, and radar echo of rain," *J. Atmos. Sci.* **5**, 161 (1948).
- ¹⁷I. V. Roisman, "Inertia dominated drop collisions. II. An analytical solution of the Navier-Stokes equations for a spreading viscous film," *Phys. Fluids* **21**, 052104 (2009).
- ¹⁸S. Popinet and S. Zaleski, "A front-tracking algorithm for accurate representation of surface tension," *Int. J. Numer. Methods Fluids* **30**, 775 (1999).
- ¹⁹L. Mahadevan and Y. Pomeau, "Rolling droplets," *Phys. Fluids* **11**, 2449 (1999).
- ²⁰H. Wagner, "Über Stoß- und Gleitvorgänge an der Oberfläche von Flüssigkeiten," *Z. Angew. Math. Mech.* **12**, 193 (1932).
- ²¹M. J. Cooker and D. H. Peregrine, "Pressure-impulse theory for liquid impact problems," *J. Fluid Mech.* **297**, 193 (1995).
- ²²C. Josserand and S. Zaleski, "Droplet splashing on a thin liquid film," *Phys. Fluids* **15**, 1650 (2003).
- ²³A. L. Yarin and D. A. Weiss, "Impact of drops on solid-surfaces—Self-similar capillary waves, and splashing as a new-type of kinematic discontinuity," *J. Fluid Mech.* **283**, 141 (1995).
- ²⁴K.-T. Yang, "Unsteady laminar boundary layers in an incompressible stagnation flow," *Trans. ASME, J. Appl. Mech.* **25**, 421 (1958).
- ²⁵L. D. Landau and E. M. Lifshitz, *Fluid Mechanics* (Pergamon, Oxford, 1984).
- ²⁶L. Prandtl, in *Gesammelte Abhandlungen*, edited by W. Tollmien, H. Schlichting, and H. Görtler (Springer, Berlin, 1961), Vol. II, pp. 575–584.
- ²⁷L. Rosenhead, *Laminar Boundary Layers* (Oxford University Press, London, 1963).
- ²⁸G. I. Taylor, "The dynamics of thin sheets of fluid III. Disintegration of fluid sheets," *Proc. R. Soc. London, Ser. A* **253**, 313 (1959).
- ²⁹F. E. C. Culick, "Comments on a ruptured soap film," *J. Appl. Phys.* **31**, 1128 (1960).
- ³⁰R. D. Schroll, C. Josserand, S. Zaleski, and W. W. Zhang, "Impact of a viscous liquid drop," *Phys. Rev. Lett.* **104**, 034504 (2010).
- ³¹A. I. Fedorchenko, A.-B. Wang, and Y.-H. Wang, "Effect of capillary and viscous forces on spreading of a liquid drop impinging on a solid surface," *Phys. Fluids* **17**, 093104 (2005).
- ³²T. Bennett and D. Poulikakos, "Splat-quench solidification: Estimating the maximum spreading of a droplet impacting a solid surface," *J. Mater. Sci.* **28**, 963 (1993).
- ³³Š. Šikalo, H. D. Wilhelm, I. V. Roisman, S. Jakirlic, and C. Tropea, "Dynamic contact angle of spreading droplets: Experiments and simulations," *Phys. Fluids* **17**, 062103 (2005).
- ³⁴M. Pasandideh-Fard, S. Chandra, and J. Mostaghimi, "A three-dimensional model of droplet impact and solidification," *Int. J. Heat Mass Transfer* **45**, 2229 (2002).
- ³⁵D. Bartolo, C. Josserand, and D. Bonn, "Retraction dynamics of aqueous drops upon impact on non-wetting surfaces," *J. Fluid Mech.* **545**, 329 (2005).
- ³⁶P.-G. de Gennes, "Wetting: Statics and dynamics," *Rev. Mod. Phys.* **57**, 827 (1985).